Unlocking the chemistry of graphene: the impact of charge carrier concentration on molecular adsorption on graphene

Maciej J. Szary[a,*]

[a]*Institute of Physics, Poznan University of Technology, ul. Piotrowo 3, 61-138 Poznan, Poland*

Abstract

Both intentional and unintentional doping of graphene is a common occurrence, as its carrier concentration can be modulated through various mechanisms. While extensively explored in electronics for achieving desirable conductivity, other aspects of doping remain largely untapped, presenting opportunities for further innovation. This study demonstrates that carrier concentration serves as a powerful and selective tool for modulating the interaction between molecular adsorbates and graphene. The effects are tunable and evident for both n-type and p-type doping, with low-to-medium modulation at doping levels of $\pm 10^{12}$ e/cm^2, and substantial enhancements, with interaction strength increases exceeding 150% and hundreds of meV, at doping levels of $\pm 10^{13}$ e/cm^2. These effects are also molecule-specific, with significant enhancements for species such as water (H$_2$O), ammonia (NH$_3$), and aluminum chloride (AlCl$_3$), while having minimal impact on species like hydrogen (H$_2$). This finding not only elucidates the fundamental chemical behavior of graphene but also provides a versatile method to tailor its surface chemistry for applications in sensors, catalysis, and electronic devices. The insights from this research pave the way for advanced material design strategies, leveraging the tunable nature of graphene's properties to optimize its interaction with various molecular species.

Keywords: 2D materials, electron and hole doping, electron availability, surface interaction mechanisms, density functional theory

1. Introduction

Graphene, a two-dimensional (2D) material, has captivated the scientific community with its extraordinary properties since its discovery. Its exceptional electrical, mechanical, and thermal properties [1–3], stemming from its unique honeycomb lattice structure, have attracted attention for a plethora of powerful applications across various fields, including energy storage and conversion [4–6], catalysis [7–9], sensing [10–12], and electronics [13, 14]. Moreover, recent advancements in sheet transfer and epitaxial growth have enabled transformative progress in graphene-based device fabrication [15–19]. Paired with refinements in characterization methods [20–22], these developments have significantly broadened the potential applications for graphene-based 2D/3D systems, propelling them towards even greater utility and innovation [23–27].

Despite the promising potential and extensive efforts, fundamental challenges persist in effectively utilizing graphene in many technological applications [28–30]. Chief among these challenges is the intricate interplay between graphene and its substrate, necessitating the mitigation of negative effects and the exploitation of positive ones, all while comprehensively understanding the impact of such interactions on the monolayer via secondary effects. For example, it is well-documented that the chemical bonding between graphene and the substrate can induce a transition in the hybridization of carbon atoms from the original sp^2 to sp^3 [31–34], resulting in significant alterations to graphene's properties. Consequently, methods of decoupling have been extensively explored [35–39]. However, even when chemically decoupled, and thus retaining the linear dispersion of their π bands, the properties of graphene remain affected. These sheets still have their carrier concentration (n) modulated by the substrate type and surface defects, with both electron and hole doping possible, typically on the order of 10^{12} and 10^{13} cm^{-2} [40–45]. However, higher values have also been reported [46, 47].

While much attention has been devoted to the influence of doping on electronic applications [48–51], other potential effects have received limited consideration. Notably, changes in carrier concentration should directly affect the charge availability on graphene's surface, which has been shown to be extremely effective in modulating adsorption interactions on other 2D materials [52–54]. Although speculative, a similar effect could occur in graphene. Given the prevalent role of carrier modulation in graphene-based 2D/3D systems, this development could prove particularly relevant, with wide-reaching implications for the application of these systems in novel technological solutions.

The molecular adsorption on graphene has been extensively investigated, with a plethora of adsorption species examined. However, such studies have generally not considered the effects of charge availability on the surface of graphene, nor its correlation with carrier concentration. In most cases, the monolayer has been considered free-standing and neutral in carrier concentration [55–59], providing little insight into the potential effect of carrier-doping enhanced activity of graphene. In other cases where substrates have been considered, results show that molecular adsorption on 2D/3D substrates is generally stronger than on 2D monolayers [60, 61]. However, the slabs used in these computations are often relatively thin and not designed to induce the experimentally-reported carrier concentrations in graphene, with this aspect not considered, and thus predicted concentrations not reported. Moreover, in such cases, the impact on adsorption encompasses several factors, making it difficult to directly associate differences in interaction solely with the availability of charge on the surface of graphene. As such, despite extensive exploration of adsorption on graphene, the potential for enhanced chemical activity via charge carrier modulation remains uncertain and potentially unaccounted for in the majority of studies.

In response to this pressing need, the present study employs density functional theory (DFT) methods in a computational approach specifically designed to elucidate the relationship between carrier concentration and adsorption interactions on graphene. In it, carrier concentration is controlled via total charge, and the effects on adsorption are examined for selected molecules with iterative changes in carrier concentration. Molecular hydrogen (H$_2$), water (H$_2$O), ammonia (NH$_3$), and aluminum chloride (AlCl$_3$) are chosen as analytes to encompass a range of interaction types, providing comprehensive insights into the effects of carrier concentration on adsorption phenomena. Through this computational approach, we aim to elucidate the intricate interplay between carrier concentration and molecular adsorption on graphene,

*Corresponding author
Email address: `maciej.szary@put.poznan.pl` (Maciej J. Szary)

1

offering valuable insights for the design and optimization of graphene-based systems in diverse applications.

2. Computational Details

Material modeling of graphene was conducted using a 2D periodic slab within a 5×5 supercell (unless otherwise specified), with vacuum region between slabs along the [001] direction. In this model, adsorption occurs solely on the upper surface of the monolayer, leaving the lower side pristine. This asymmetry results in a dipole moment perpendicular to the surface, caused by charge transfer between the adsorbates and the graphene sheet. Due to the periodic boundary conditions, this configuration creates an artificial electric field between neighboring slabs. To counteract this effect, a dipole correction layer (DCL) was introduced in the middle of the vacuum region [62]. Therefore, to accommodate the DCL without it overlapping with the adsorption region above the monolayers, the vacuum width was set at approximately 25 Å.

All computations for this study employed DFT with pseudopotentials, plane waves, and the projector-augmented wave (PAW) method, as implemented in the QUANTUM ESPRESSO code [63–65]. The pseudopotentials included scalar-relativistic and nonlinear core corrections. The cutoff energies for the wavefunctions and charge density were set at 60 Ry and 500 Ry, respectively. Brillouin zone integration of the supercell utilized a Monkhorst-Pack grid of 4×4×1 [66]. Tests were carried out to evaluate the optimal cutoff energies and k-point grids, revealing that higher values had minimal effect on the modeled properties. During structure optimization, all atom positions were adjusted until the forces reached a convergence criterion of less than 10^{-4} Ry/au and the total energy reached a convergence criterion of less than 10^{-5} Ry. The Perdew-Burke-Ernzerhof (PBE) functional was employed for approximating the electron exchange–correlation energy [67, 68], as it produced comparable results to the more computationally expensive Heyd-Scuseria-Ernzerhof (HSE) hybrid functional [69] during the testing phase of the project.

Carrier density in the model systems was controlled by modulating the total charge. Consequently, all computations were executed with unrestricted spin due to some model scenarios having an odd number of electrons. The estimation of partial charges was carried out using Löwdin population analysis. All atomic schematics depicted in Figures 3, 5, 7, and 9 were generated using the XcrySDen program [70].

3. Results and Discussion

3.1. Impact of doping on intrinsic properties of graphene

Freestanding graphene is well-known for its exceptional carrier mobility, stemming from the linear energy-momentum dispersion of its π bands (see Figure 1b). These electronic bands form both the maximum of the valence band and the minimum of the conduction band, meeting at the Dirac point (E_D). In freestanding graphene, the Dirac point coincides with the Fermi energy (E_F), resulting in high resistance due to the minimal availability of charge carriers. However, as the carrier concentration increases through the addition of electrons (n-type doping) or holes (p-type doping), the Fermi level shifts away from the Dirac point, leading to an increase in the density of states at the Fermi level. This results in a greater number of available charge carriers, thereby reducing the resistance.

In n-type graphene, the electron population increases, leading to a Fermi level shift above the Dirac point (see Figure 1a), where conduction is primarily due to electrons. Conversely, in p-type graphene, the Fermi level moves below the Dirac point (see Figure 1c), and holes become the dominant charge carriers. Given the symmetrical shape of the π bands near the Dirac point, opposite values of the Fermi shift correspond to comparable levels of electron and hole doping, respectively (see Figure 1d). This ambipolarity allows for versatile electronic applications and is crucial for the design of graphene-based devices, impacting conductivity, mobility, and overall electronic behavior. Consequently, the focus on the electronic implications dominates considerations of the effects of carrier concentration in graphene. However, such doping may also facilitate secondary effects by modulating properties beyond just work function and carrier concentration. This could be particularly impactful since charge carrier modulation is quite common in graphene, arising from multiple sources.
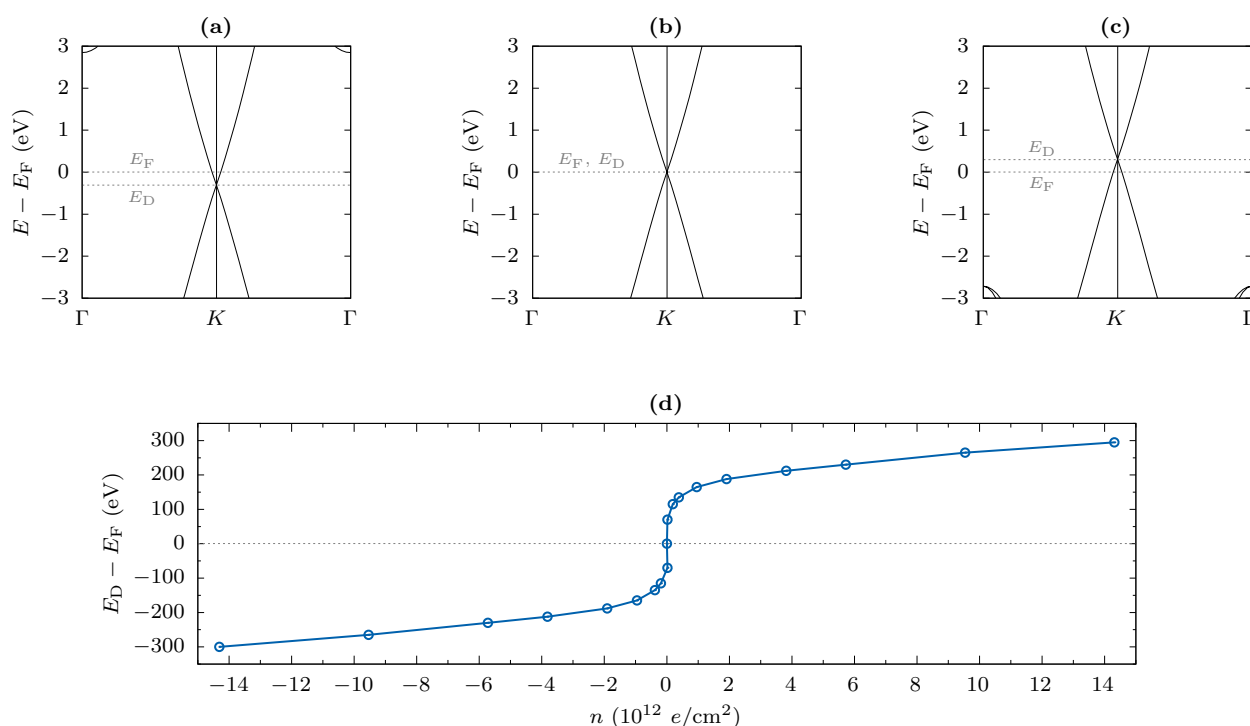

Figure 1: Electronic band structures of graphene when (a) n-doped, (b) neutral, and (c) p-doped. (d) Difference between the Dirac-point and Fermi energies. Results were obtained from calculations for an unit cell of graphene. Carrier concentrations in panels (a) and (c) are -1.43 and 1.43×10^{13} e/cm^2, respectively.

The primary sources of graphene doping include self-doping induced by intrinsic defects, substrate bulk doping, and spontaneous polarization. Self-doping arises from charge accumulation near defects, such as vacancies or adsorbates [71]. Substrate bulk doping depends on the specifics of band bending at the surface, which is influenced by the type and concentration of bulk dopants, determining the location of the chemical potential within the band gap [72]. Spontaneous polarization arises in dielectric crystals where dipole distributions align along the surface normal. Within the bulk phase, periodic boundary conditions ensure a net zero electric field across the unit cell. However, at the surfaces, translation symmetry is disrupted, allowing the dipoles to accumulate and create an uncompensated polarization field. This spontaneous polarization leads to a pseudo-charge at the surface, akin to an acceptor layer, which can cause significant doping [73].

The doping should be intrinsically linked with the charge availability on graphene surfaces. This is because the π bands, which form the valence band maximum and conduction band minimum, consist exclusively of the carbon $2p(z)$ orbitals. Consequently, any alteration in charge carrier concentration directly impacts their electron population. The C $2p(z)$ orbitals extend outward and are geometrically available for interaction with adsorbates. In contrast, the $2p(x)$ and $2p(y)$ orbitals of carbon are predominantly confined to the plane of the monolayer, exhibiting limited outward projection. Therefore, changes in carrier concentration in graphene should disproportionately affect charge availability, with n-type doping increasing and p-type doping decreasing it. This variation is likely to influence the chemical activity of graphene surfaces, as charge availability has been reported as a potent mechanism for modulating surface interactions in other 2D materials [52–54].

Due to the common charge-transfer mechanisms on graphene across different doping levels, the charge availability on its surfaces can be evaluated by inspecting the planar averages of its total electron density against distance (avg. $\rho(z)$). Hence, to examine the impact of carrier concentration on charge availability, we compare the planar averages for doped and neutral sheets, as illustrated in Figure 2. The data is presented for varying carrier concentrations, indicated by the color gradient from red to blue. Red hues represent n-doped graphene, whereas blue hues represent p-doped graphene. The chosen range of carrier concentrations aims to reflect common doping levels in the sheet [40–45].

Findings reveal the significant influence of carrier concentration on charge availability on graphene surfaces. In n-doped graphene (red hues), the average electron-density difference is higher near the graphene surface, decreasing as the distance increases. Conversely, for p-doped graphene (blue hues), the difference in density is lower near the surface and increases with distance. The magnitude of these differences correlates systematically with the carrier concentration. At the highest doping levels ($\pm 7.57 \times 10^{13}$ e/cm^2), the electron density difference at 1 Å from the surface reaches $\pm 4.33 \times 10^{-4}$ e/au^3, whereas at the lowest doping levels ($\pm 0.76 \times 10^{13}$ e/cm^2), this difference is only $\pm 0.43 \times 10^{-4}$ e/au^3. However, at both doping levels, these differences decrease to nearly zero around 3.5 Å away from the graphene plane. The symmetry of the graph implies that both n-doping and p-doping introduce comparable but opposite changes in electron density. Positive values (above the neutral plane) signify increased electron availability due to n-doping, while negative values (below the neutral plane) indicate reduced electron availability due to p-doping. The most substantial charge redistribution occurs near the graphene surface, tapering off rapidly away from it. This behavior suggests that the functional impact of doping on electronic properties is highly localized near the graphene sheet, potentially exerting a significant influence on the chemical activity of graphene surfaces.

3.2. Interplay between carrier concentration in graphene and its chemical activity

Given that carrier concentration effectively modulates charge availability on graphene, it is crucial to examine how this effect influences interactions on its surface. However, these effects may vary depending
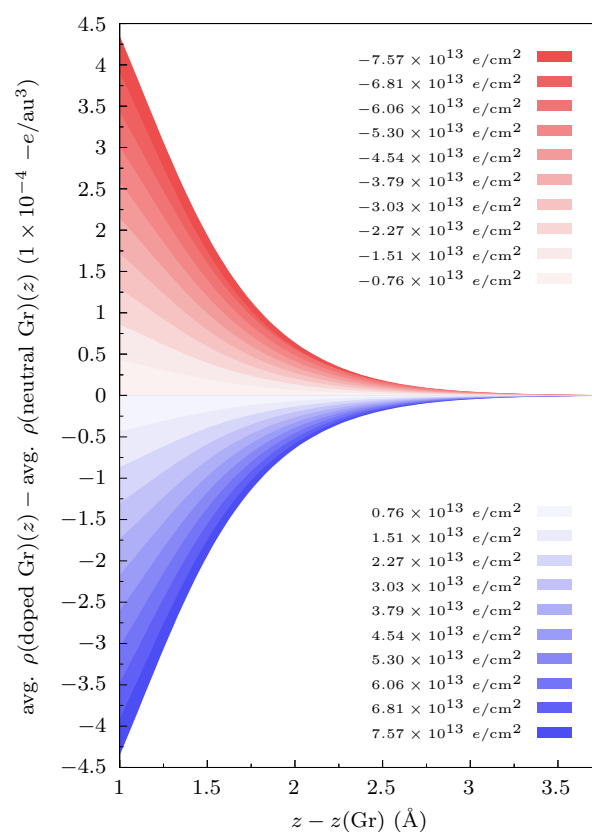

Figure 2: The differences in planar averages of the total electron density between doped and neutral sheets plotted against distance from graphene. Varying carrier concentrations are indicated by the color gradient changing from red to blue. Red hues represent n-doped graphene with increasing electron concentration, whereas blue hues represent p-doped graphene with increasing hole concentration.

on the adsorbate's dominant interaction mechanism. Therefore, it is essential that the chosen analytes have the propensity to facilitate different interaction modes with graphene. For this purpose, four molecular species have been selected. H_2 generally favors weak physisorption dominated by vdW forces, lacking an intrinsic dipole moment and having limited potential for its induction. In contrast, H_2O has an intrinsic dipole moment of 1.85 D and the potential for hydrogen bonding. NH_3, with a dipole moment of 1.42 D, is a Lewis base with a filled orbital containing an electron pair that can be shared with acceptor species (Lewis acids) to form a dative bond. Finally, $AlCl_3$ has an empty orbital capable of accepting an electron pair from donor species (Lewis bases), making it prone to dative bonding as a Lewis acid.

Considering that some interactions may require specific adsorption configurations, the adsorption of molecular species was evaluated at two adsorption sites: one on top of a carbon atom of graphene and the other centered above a hexagonal ring. Additionally, two molecular configurations were considered for each adsorbate (except $AlCl_3$), resulting in fourteen distinct adsorption systems. These systems were examined on neutral graphene as well as on twenty doped sheets (ten n-type and ten p-type) at varying doping levels. Altogether, this effort presents 294 distinct adsorption cases.

3.2.1. Effects for H_2

To assess the impact carrier concentration has on the chemical activity of graphene, it is crucial to first characterize the molecule-sheet interactions. Following the methodology employed in other studies [52–59], this is primarily quantified by calculating the adsorption energy, which can be expressed as:

$$E_{ads} = E(\text{mol.@MLG}) - E(\text{free mol.}) - E(\text{free MLG}), \quad (1)$$

3
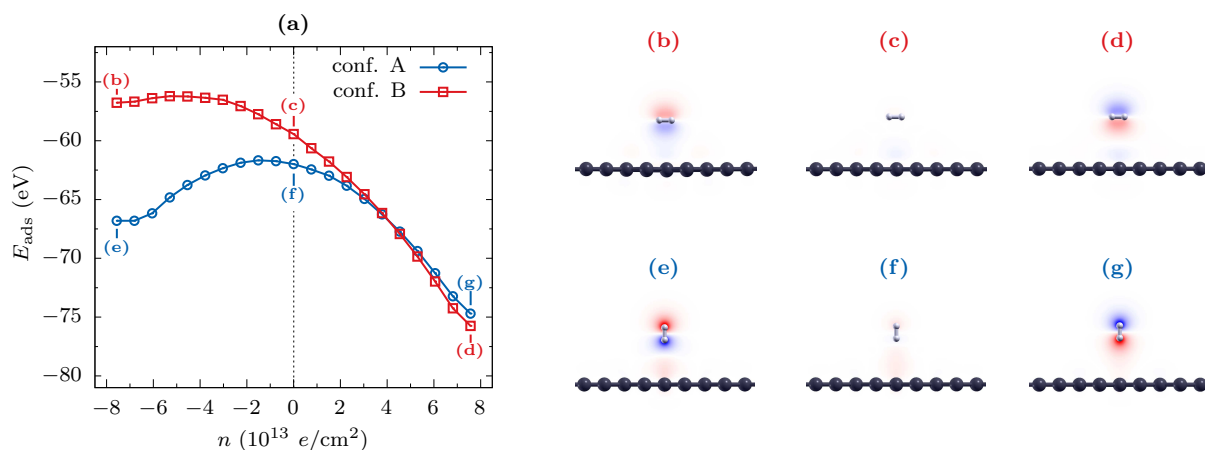
Figure 3: (a) Adsorption energy of H_2 on graphene calculated using Equation (1). Change in electronic density resulting from adsorption in configurations (b–d) B and (e–g) A, given by Equation (2). Red indicates electron accumulation, wheres blue a depletion.

where $E(\text{mol.@MLG})$, $E(\text{free mol.})$, and $E(\text{MLG})$ represent the total energy of the adsorbate-substrate system, free molecule, and monolayer graphene, respectively.

Figure 3a illustrates the evolution of the adsorption energy of H_2 on graphene as a function of the sheet's carrier concentration. The results are shown for two configurations: configuration A, where the molecule is oriented vertically over a carbon atom, and configuration B, where the molecule is oriented horizontally above it. The configurations centered at the hexagonal ring are not included, as the interaction with H_2 is primarily dominated by vdW forces, making it dispersive in nature. Consequently, the lateral position of the molecule does not significantly affect the interaction characteristics, providing no additional insight into the impact of carrier concentration on adsorption.

The results reveal that carrier concentration in graphene affects the adsorption of H_2 on its surface, although the effect is relatively limited and depends on the molecular orientation and the type of doping. For a neutral sheet, the adsorption energy is −62 meV for configuration A and −59 meV for configuration B. In configuration A, the adsorption energy generally becomes more negative (indicating stronger binding) as the concentration increases towards both higher positive and negative doping values, reaching −67 meV and −75 meV at -7.57×10^{13} e/cm^2 and 7.57×10^{13} e/cm^2, respectively. The exception are the concentrations around of -1.5×10^{13} e/cm^2 where the interaction weakens slightly. In configuration B, the adsorption energy exhibits a similar but steeper trend with increasing hole concentration, becoming more energetically favorable around carrier concentrations of 4×10^{13} e/cm^2 and reaching −76 meV at 7.57×10^{13} e/cm^2. Conversely, electron doping generally destabilizes the adsorption of hydrogen, with adsorption energies higher than those on a neutral sheet.

To better understand the underpinnings of these changes, it is prudent to inspect the redistribution of charge resulting from molecule-sheet interactions. This can be assessed by calculating the total charge density of the adsorption system, denoted as $\rho(\text{mol.@MLG})$, and subtracting the charge densities of its individual constituents.

$$\delta\rho = \rho(\text{mol.@MLG}) - \rho(\text{ free mol.}) - \rho(\text{MGL}). \quad (2)$$

The results demonstrate that the adsorption of H_2 on neutral graphene results in minimal charge redistribution, which indicates a lack of substantial dipole induction upon adsorption (see Figures 3c and 3f). This somewhat changes for doped sheets, where a more significant redistribution of charge occurs in the vicinity of the molecule. For n-doped graphene, charge polarization in the sheet leads to a depletion of electronic density between H_2 and graphene, with an accumulation of charge near the molecule away from the sheet (Figures 3b and 3e). In contrast, for p-doped graphene, the polarization is opposite, and thus charge redistribution becomes reversed (Figures 3d and 3g). This dif-
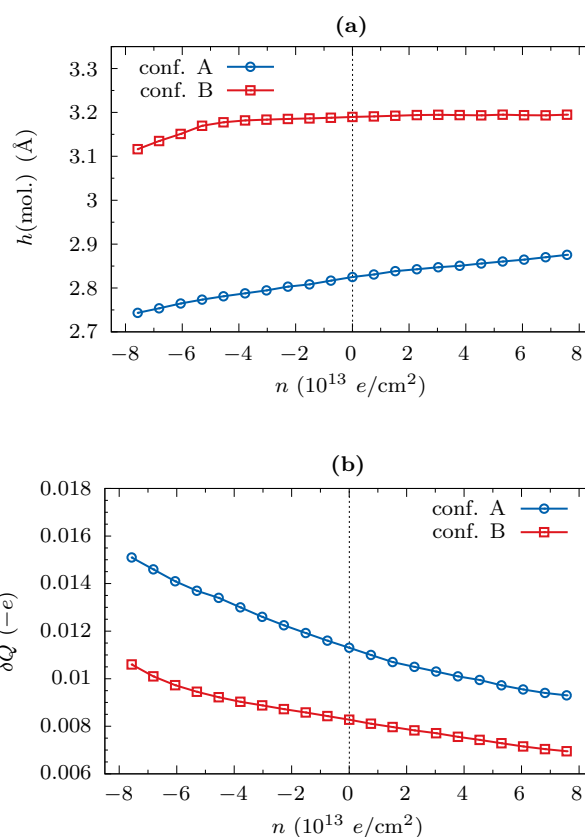

Figure 4: (a) Vertical separation of the molecule from the graphene. (b) Charge transfer between H_2 and graphene given by Equation (3).

ference is likely responsible for the variation in adsorption energy between doping types since the accumulation of charge between the adsorbate and the substrates should facilitate a stronger interaction. That said, it should be emphasized that this dipole formation has a limited impact on the overall strength of the molecule-sheet interaction, with its energy changing by only 15 meV or less.

The low impact of doping is also reflected in the molecule-sheet distances (see Figure 4a). The vertical separations between H_2 and neutral graphene in configurations A and B are 2.82 Å and 3.19 Å, respectively, with doping introducing variations of 0.07 Å or less. These distances align with the weak adsorption of H_2, and the variation remains particularly low in comparison.

It is also crucial to emphasize that the redistribution of electronic

density near H_2, seen in Figures 3b–g, does not equate to charge transfer between the molecule and the graphene sheet. Rather, the minimal change in electronic density near graphene (see Figure 3) suggest limited transfers. Consequently, this aspect of the interaction warrens further clarification. By calculating the charge transfer, given by

$$\delta Q = Q(\text{mol.@MLG}) - Q(\text{free mol.}), \qquad (3)$$

where $Q(\text{mol.@TMD})$ and $Q(\text{free mol.})$ are the net charges of the adsorbed and free molecule, respectively, it becomes evident that its values are very low for neutral graphene and remain low for doped sheets (see Figure 4b). This indicates that H_2 does not become partially charged upon adsorption despite doping, and thus, there is no additional electrostatic component to the interaction. Therefore, the interaction is predominantly influenced by the dipole moment induced in the molecule, rendering the effects of carrier concentration in graphene somewhat ineffective in modulating H_2 adsorption.

3.2.2. Effects for H_2O

Figure 5a illustrates the evolution of the adsorption energy for H_2O as a function of graphene's carrier concentration. The results are shown for two configurations: A, where the molecule is oriented vertically with its hydrogen atoms facing graphene, and B, where its oxygen atom faces the sheet. Both configurations are centered above a carbon atom in graphene. The positioned at the hexagonal ring are not included, as the interactions with H_2O are strongly dispersive, making different lateral positions of the molecule result in qualitatively equivalent interactions.

The results reveal a significant modulation of the adsorption interaction through sheet doping, with a strong interplay between molecular orientation and doping type. For neutral graphene, configuration A is more favorable, with an adsorption energy of -125 meV. This interaction is characterized by a notable charge accumulation below the molecule, dispersed over a relatively large area of the graphene surface, electron depletion between hydrogen atoms, and an accumulation centered on the oxygen atom of the molecule (see Figure 5f). This interaction is further enhanced on n-type graphene, where the adsorption energy of H_2O scales linearly with the electron concentration in the sheet, reaching -299 meV at -7.57×10^{13} e/cm^2 (see Figure 5a).

In this scenario, n-type doping enhances the intrinsic molecular-sheet interaction rather than altering it, as indicated by differences in electron densities shown in Figures 5e and 5f. Comparing these panels reveals that interactions on both neutral and electron-doped graphene follow the same pattern of charge redistribution, which is simply intensified on n-type graphene. This intensification is likely facilitated by the excess electronic charge in the doped sheet, making electrons more readily available to accumulate on the surface of graphene below

(a)

(b)

Figure 6: (a) Vertical separation of the molecule from the graphene. (b) Charge transfer between H_2O and graphene given by Equation (3).

the molecule. This, in turn, induces a more pronounced polarization in H_2O, enhancing the interaction. This enhancement is further evidenced by a reduction in the molecule-sheet distance from 2.73 Å for neutral graphene to 2.58 Å at a doping level of -7.57×10^{13} e/cm^2 (see Figure 6a), and an increase in electron transfer to the molecule from -0.009 e to -0.016 e (see Figure 6b).

Conversely, this adsorption is destabilized on p-type graphene as its energy increases, and at 3.79×10^{13} e/cm^2, the molecule spontaneously flips into configuration B. This effect is associated with a reversal in charge redistribution, where electrons accumulate on hydrogen atoms, and there is minor depletion near oxygen (see Figure 5g). This likely occurs because such redistribution opposes the intrinsic polarization in the molecules, and although it still coincides with electronic accumu-
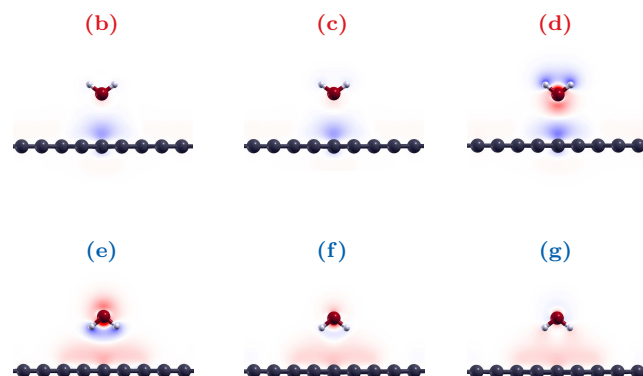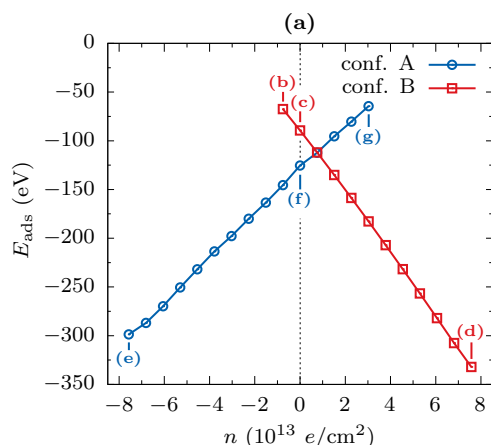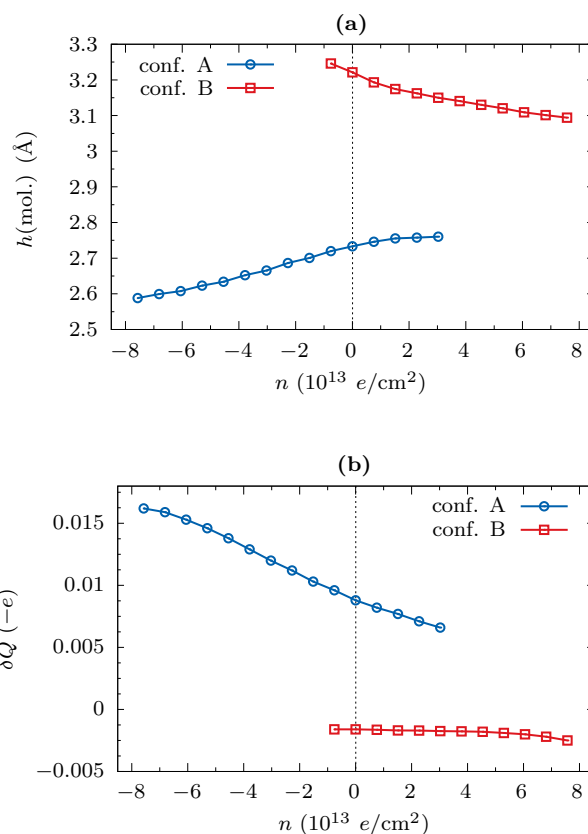

Figure 5: (a) Adsorption energy of H_2O on graphene calculated using Equation (1). Change in electronic density resulting from adsorption in configurations (b–d) B and (e–g) A, given by Equation (2). Red indicates electron accumulation, wheres blue a depletion.

5

lation on the graphene surface, electrons are less available due to the hole doping of the sheet. Consequently, the resulting destabilization is accompanied by increased molecule-sheet distances (see Figure 6a) and reduced charge transfers (see Figure 6b).

Interestingly, the effects of doping on the adsorption of H_2O in configuration A are reversed for configuration B. For neutral graphene, B-type adsorption is less favorable, with an energy of -89 meV. This interaction results in charge depletion on the graphene surface directly below H_2O and accumulation on the oxygen atom of the molecule (see Figure 5c). The adsorption is quickly destabilized on n-type graphene, as its energy increases linearly (see Figure 5a), coinciding with limited effects on charge redistribution (see Figure 5b) and charge transfer (see Figure 6b), but an increase in molecule-sheet distance (see Figure 6a). Consequently, at -1.51×10^{13} e/cm^2, the molecule spontaneously flips into configuration A. This destabilization is likely facilitated by the negatively charged oxygen atom in H_2O still necessitating an electronic depletion below the molecule despite the electron doping.

In contrast, B-type adsorption is enhanced on p-type graphene. In this case, hole doping increases the intrinsic molecular-sheet interaction rather than altering it. This is indicated by differences in electron densities shown in Figures 5c and 5d. A comparison of these panels reveals that interactions on both neutral and hole-doped graphene follow the same pattern of charge redistribution, which is intensified on p-type graphene. This intensification is likely facilitated by the lack of electronic charge in the doped sheet, making holes more readily available to accumulate on the surface of graphene below the molecule. As a result, this induces a more pronounced polarization in the molecule, enhancing the interaction. This enhancement is reflected in the adsorption energy of H_2O, which scales linearly with the hole concentration in the sheet, reaching -332 meV at 7.57×10^{13} e/cm^2 (see Figure 5a). It also affects the molecule-sheet distance, reducing it from 3.22 Å for neutral graphene to 3.09 Å at a doping level of 7.57×10^{13} e/cm^2 (see Figure 6a). However, the effects on charge transfer are negligible (see Figure 6b).

Taken together, the results reveal that carrier concentration effectively modulates the orientation of water molecules on graphene. On the neutral sheet, H_2O adopts both A- and B-type configurations, with a statistical tendency toward orientations with hydrogen atoms facing graphene. Conversely, n-type doping predominantly facilitates A-type configurations, while p-type doping favors B-type configurations. This insight could help engineer catalytic processes that require specific orientations of water molecules or benefit humidity monitoring.

3.2.3. Effects for NH$_3$

Figure 7a depicts the variation in NH$_3$ adsorption energy as a function of the carrier concentration in graphene. The data is presented for two distinct configurations: in configuration A, the NH$_3$ molecule is oriented vertically with its hydrogen atoms directed toward the graphene surface, while in configuration B, the nitrogen atom faces the sheet. Both configurations have the molecule centered above a carbon atom. The configurations with NH$_3$ positioned over the hexagonal ring are excluded due to the dominance of dispersive interactions with NH$_3$, resulting in qualitatively similar adsorption regardless of the molecule's lateral position.

The results reveal a sizable modulation of the adsorption interaction through sheet doping with a strong correlation between NH$_3$ orientation and the doping type, analogous to H_2O. For neutral graphene, configuration A is more favorable, with an adsorption energy of -125 meV. This interaction involves minimal charge redistribution, with negligible electronic charge accumulation on nitrogen in NH$_3$ and slight depopulation on the graphene surface (see Figure 7g). This the adsorption is then enhanced on n-type graphene, where its energy decreases nearly linearly with electron concentration up to -6.06×10^{13} e/cm^2, reaching -231 meV (see Figure 7a). The electron doping modulates the molecular-sheet interaction, leading to increased electronic charge accumulation near nitrogen and more substantial depletion below the molecule (compare Figures 7f and 7g). The enhanced interaction is likely facilitated by excess electronic charge in the doped sheet, inducing more pronounced polarization in the molecule. This is further evidenced by a reduction in the molecule-sheet distance from 3.13 Å for neutral graphene to 3.03 Å (see Figure 8a) and a minor increase in electron transfer to the molecule from -0.005 e to -0.008 e (see Figure 8b). For electron concentrations beyond -6.06×10^{13} e/cm^2, the increase in interaction strength slows substantially (see Figure 7a), coinciding with a slower decrease in the molecule-sheet distance. Interestingly, this shift does not correspond with significant changes in charge redistribution due to the molecule-sheet interaction (compare Figures 7e and 7f), suggesting potential saturation in NH$_3$ polarization and thus reduced effectiveness in modulating adsorption by electron doping.

Conversely, NH$_3$ adsorption becomes destabilized on p-type graphene, with the adsorption energy increasing nearly linearly up to a hole concentration of 5.3×10^{13} e/cm^2, reaching -63 meV at that point. This destabilization is associated with a reversal in charge redistribution around the molecule, where electrons accumulate on the hydrogen atoms, and there is a minor depletion near the nitrogen (see Figure 7h), similar to the p-doping effects observed for H_2O. This redistribution likely opposes the intrinsic polarization of NH$_3$, reducing its dipole moment. Consequently, the destabilization is accompanied by increased molecule-sheet distances (see Figure 8a) and a slight reduction in charge transfer (see Figure 8b).

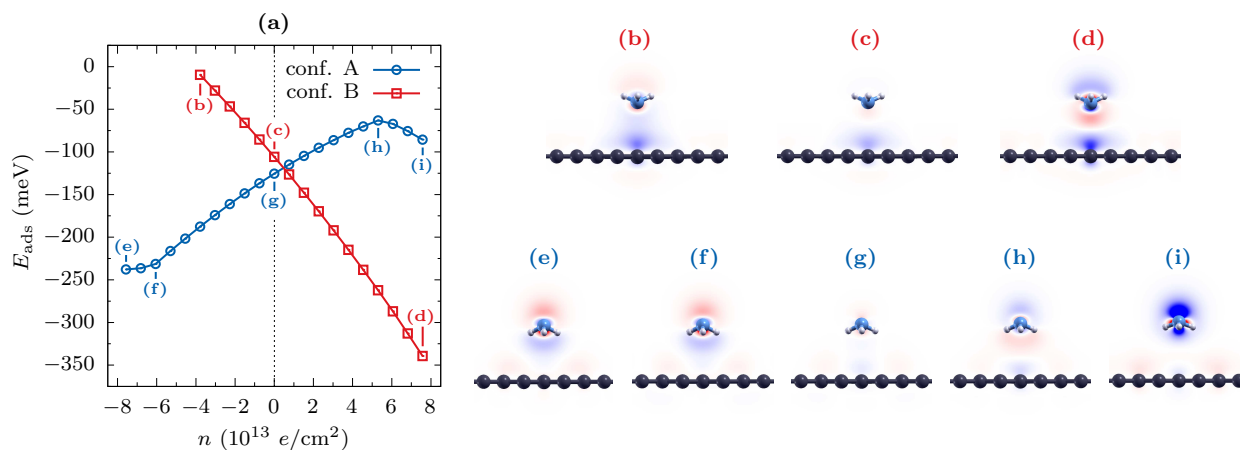However, beyond a hole concentration of 5.3×10^{13} e/cm^2, the

Figure 7: (a) Adsorption energy of NH$_3$ on graphene calculated using Equation (1). Change in electronic density resulting from adsorption in configurations (b–d) B and (e–i) A, given by Equation (2). Red indicates electron accumulation, wheres blue a depletion.
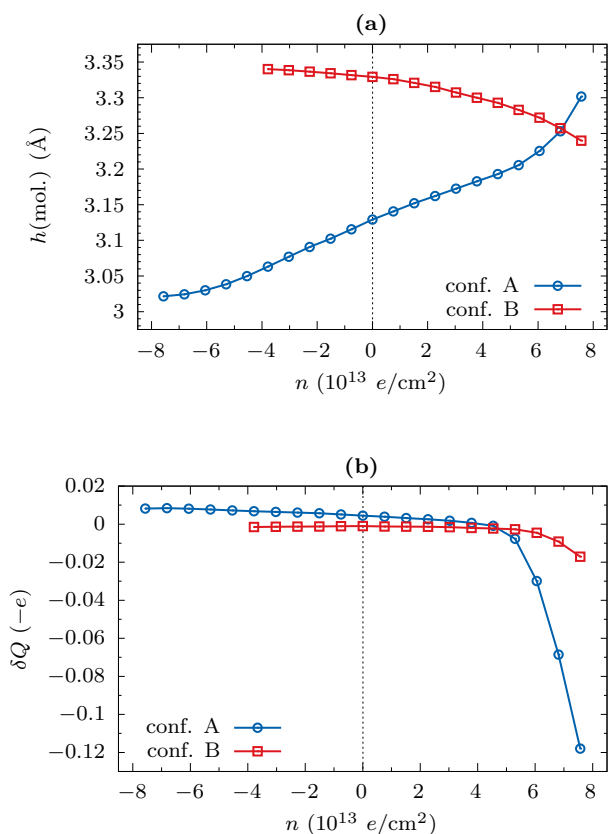
6

Figure 8: (a) Vertical separation of the molecule from the graphene. (b) Charge transfer between NH_3 and graphene given by Equation (3).

adsorption energy of NH_3 begins to decrease, breaking the previous trend. This coincides with a rapid change in charge transfer, where the molecule donates up to -0.118 e to the graphene (see Figure 8b), and a substantial decrease in electronic density near the nitrogen atom in NH_3 (see Figure 7i). This effect is likely facilitated by the reduced electronic charge in the doped sheet, making substantial electron transfer to the graphene favorable despite the initial adsorption configuration. As a result, the molecule becomes charged, enhancing electrostatic interactions.

For neutral graphene, the adsorption energy in configuration B is -106 meV (see Figure 7a). This interaction is characterized by electron accumulation on the nitrogen atom, minimal depletion on the hydrogen atoms, and pronounced depletion on the graphene surface beneath the molecule (see Figure 7c). Unlike configuration A, n-type doping destabilizes adsorption in configuration B. The adsorption energy increases nearly linearly with electron concentration, leading to complete destabilization above -4.54×10^{13} e/cm^2. Moreover, there is also a systematic increase in the molecule-sheet distances (see Figure 8a). The destabilization is associated with changes in charge redistribution: electrons accumulate on the hydrogen atoms, less on the nitrogen, and there is intensified depletion on the graphene surface (see Figure 7g). As such, this likely occurs because the redistribution opposes the intrinsic polarization of the molecule, and in addition requiring more hole accumulation on the graphene surface despite electron doping.

In contrast, B-type adsorption on p-type graphene demonstrates an energy that scales almost linearly with hole concentration, reaching -339 meV at 7.57×10^{13} e/cm^2. This effect is associated with hole doping enhancing the intrinsic interaction between the molecule and the graphene sheet rather than changing it, as indicated by the electron density differences shown in Figures 7c and 7d. A comparison of these figures shows that the interactions on both neutral and hole-doped graphene follow the same pattern of charge redistribution, but it is more pronounced on p-type graphene. This is likely facilitated by the excess

holes in the doped sheet, enabling a more significant depletion of electrons on the graphene surface beneath the molecule. As a result, there is greater polarization in the molecule, which enhances the interaction. The enhancement is further evidenced by a reduction in the molecule-sheet distance from 3.33 Å for neutral graphene to 3.24 Å at a doping level of 7.57×10^{13} e/cm^2 (see Figure 8a), and an increase in electron transfer to the sheet from -0.001 e to -0.017 e (see Figure 8b).

Taken together, the results reveal that carrier concentration modulates the orientation of NH_3 molecules on graphene. The effects are similar to those observed for H_2O; however, due to the atomic structure of NH_3, carrier concentration is less effective in destabilizing its adsorption.

3.2.4. Effects for $AlCl_3$

Figure 9a illustrates the evolution of the adsorption energy of $AlCl_3$ on graphene as a function of the sheet's carrier concentration. The results are presented for two configurations: configuration A, where the molecule is oriented flat with the aluminum in $AlCl_3$ directly above a carbon atom, and configuration B, where it is centered above the hexagonal ring of the graphene sheet.

For neutral graphene, configuration A is more favorable, with an adsorption energy of -457 meV. This interaction is notably stronger than those previously considered, due to $AlCl_3$'s propensity for dative bonding when interacting species can share their lone pair electrons. While the 2p(z) orbitals of carbon are not fully occupied in graphene, only those that can effectively overlap with aluminum orbitals are needed for dative bonding. This results in a charge transfer within graphene to increase the population in the 2p(z) orbitals of selected carbon atoms, as indicated by a substantial accumulation of electronic charge between aluminum in $AlCl_3$ and the carbon atom directly below it (see Figure 9g). This coincides with a dispersed decrease in electronic density on the graphene surface, indicating charge transfers, and additional accumulation on chlorine atoms, originating from a nonnegligible electron transfer to $AlCl_3$ of -0.072 e.

That said, a fully-formed dative bond would generally result in lower adsorption energies for $AlCl_3$ than observed on neutral graphene [74], and its covalent nature would also demand a shorter molecule-sheet distance than the 3.17 Å observed here. Furthermore, forming a dative bond would require aluminum to transition from a flat sp^2 hybridization to a pyramidal sp^3, resulting in a visible change in the molecule's atomic structure. However, upon adsorption on neutral graphene, $AlCl_3$ remains relatively flat, with Cl atoms shifting only 0.18 Å above Al, indicating nearly sp^2-hybridized Al, and thus limited effectiveness of dative bonding.

The limited effectiveness of the dominant bonding mechanism enables this interaction to be effectively modulated by electron doping of graphene. The excess electrons facilitate their transfer into the 2p(z) orbitals of carbon atoms directly facing the molecule, as indicated by a substantial increase in electronic density between the aluminum and carbon atoms (see Figure 9f). This significantly enhances the interaction, resulting in an adsorption energy of -723 meV at a concentration of -7.57×10^{13} e/cm^2 (see Figure 9a), accompanied by a reduction in the molecule-sheet distance to 2.36 Å (see Figure 10a) and a notably elevated electron transfer of -0.354 e (see Figure 10b). Additionally, the effects of this interaction are evident in the structure of the molecule and the graphene sheet. At -7.57×10^{13} e/cm^2, Cl atoms in the adsorbed $AlCl_3$ shift 0.64 Å above Al, indicating a more sp^3-hybridized Al (see Figure 10c). Similarly, the adsorption causes the carbon atom bonding with aluminum to shift 0.34 Å above the neighboring atoms in the sheet, indicating that the dative bonding also alters the hybridization in graphene, making it more sp^3 in one of its atoms (see Figure 10d).

It should be emphasized that electron doping enhances the intrinsic molecular-sheet interaction but does not change its mechanisms, as indicated by differences in electron densities shown in Figures 9f and 9g. Comparing these panels reveals that interactions on both neutral
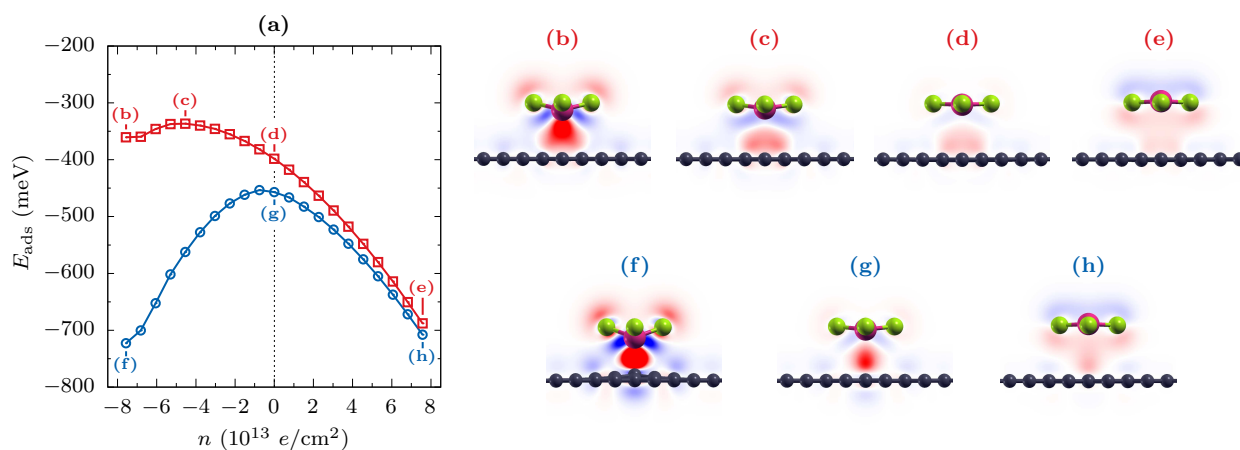
7

Figure 9: (a) Adsorption energy of AlCl$_3$ on graphene calculated using Equation (1). Change in electronic density resulting from adsorption in configurations (b–e) B and (f–h) A, given by Equation (2). Red indicates electron accumulation, wheres blue a depletion.

and electron-doped graphene follow the same pattern of charge redistribution, which is simply intensified on n-type graphene.

Conversely, hole doping of graphene alters the adsorption mechanism of AlCl$_3$, as it does not facilitate an increased electron population in the 2p(z) orbitals of carbon; rather, it works against it. In this scenario, the interaction breaks the planar symmetry of the molecule. The Cl atoms face the sheet, with Al shifting above them (see Figure 10c). This change results in electron depletion above the molecule and accumulation below it, coupled with accumulation on the graphene surface directly beneath the molecule and more dispersed depletion elsewhere on the surface (see Figure 9h). This indicates that the interaction becomes more dispersive, with increased interaction strength (see Figure 9a) likely stemming from enhanced electrostatic attraction between positively charged graphene and negatively charged Cl atoms in AlCl$_3$.

Given the directional nature of the dative bonding, the adsorption site notably affects its potential. For neutral graphene, the adsorption energy in configuration B is −398 meV (see Figure 9a). This interaction exhibits a charge redistribution pattern similar to configuration A, but the position of the molecule causes the accumulation below to be more dispersed, overlapping with several neighboring carbon atoms (see Figure 9d). Excess electrons in n-type graphene facilitates a charge transfer into the 2p(z) orbitals of carbon atoms, increasing the electronic density between the aluminum and carbon atoms in configuration B (see Figure 9c). However, unlike in configuration A, n-type doping destabilizes the adsorption. This likely occurs because the interactions become more dative, but the aluminum position requires a four-center two-electron bond, which is at odds with the hybridization in graphene. This trend reverses only for electron concentrations above −5.3 × 10^{13} e/cm^2 (see Figure 9a), coinciding with a substantial increase in charge transfers (see Figure 10b). This suggests that only at sufficiently high populations of 2p(z) orbitals does the more dative-like interaction become feasible. However, because several neighboring carbon atoms are involved, the resulting electronic charge accumulation below the molecule becomes more dispersed (compare Figures 9b and 9f). On the other hand, p-type doping of graphene favors a more dispersed interaction character. Therefore, for p-type graphene, adsorption in configurations A and B becomes qualitatively identical, with comparable adsorption energies (see Figure 9a), molecule-sheet distances (see Figure 10a), charge transfers (see Figure 10b), molecule deformation (see Figure 10c), graphene corrugation (see Figure 10d), and charge redistribution (compare Figures 9e and 9h).

Overall, the results reveal that doping of graphene can effectively modulate the adsorption of AlCl$_3$. Both doping types enhance the interaction, but n-type doping makes one adsorption site notably more favorable, while p-type doping makes different sites more equivalent. Consequently, n-type graphene should facilitate more uniform adsorp-

tion of AlCl$_3$ compared to p-type sheets.

3.3. Significance of doping at different doping level

As demonstrated in section 3.2, sheet doping can significantly impact interactions with graphene, though the effects vary between adsorbates and doping levels. This means that, while doping generally influences interactions, its relevance can range, with the potential for both negligible and major implications for practical applications of graphene. Therefore, it is essential to assess the significance of doping and consider how impactful it can be at key levels.

For this purpose, two doping regimes will be examined. One will quantify the impact of doping on adsorption when on the level of 10^{12} e/cm^2, and the other at 10^{13} e/cm^2. The analysis will focus on adsorption energy, as it is the primary indicator of interaction modulation. Moreover, changes in adsorption energy impact macroscopic properties such as sheet adsorption coverage and sensitivity [54]. To evaluate the significance of modulation, both absolute and relative changes in adsorption energy will be examined, using formulas

$$\Delta(\text{ads.}) = \left| E_{\text{ads}}(\text{doped}) - E_{\text{ads}}(\text{neutral}) \right|, \tag{4}$$

$$\Delta(\text{rel.}) = \left| \frac{E_{\text{ads}}(\text{doped}) - E_{\text{ads}}(\text{neutral})}{E_{\text{ads}}(\text{neutral})} \right|, \tag{5}$$

where $E_{\text{ads}}(\text{doped})$ and $E_{\text{ads}}(\text{neutral})$ are the adsorption energies on doped and neutral graphene. The former, represent the values at the doping levels of ±0.76 or ±7.57 × 10^{13} e/cm^2.

Table 1 summarizes the absolute and relative changes in the adsorption energy of the investigated species between different doping regimes. The results demonstrate that doping levels on the order of 10^{12} e/cm^2 have virtually no impact on the adsorption of H$_2$, with both n-type and p-type doping resulting in less than a 1% change, corresponding to less than 1 meV in adsorption energy. The effect is somewhat enhanced at doping levels on the order of 10^{13} e/cm^2. In this regime, n-type doping results in a 4% modulation, while p-type doping leads to a more substantial 22% change. However, it should be emphasized that these relative changes correspond to variations of only 3 meV and 14 meV, respectively. Hence, in most practical cases, the effects of doping on the adsorption of H$_2$ should be considered generally low on graphene. Moreover, given the mechanism by which the doping affects the interaction with H$_2$, modulation for N$_2$ and O$_2$ may also be somewhat limited.

In contrast, doping is about ten times more effective in modulating the adsorption of H$_2$O and NH$_3$. The results demonstrate that even at doping levels on the order of 10^{12} e/cm^2, it can result in changes of 16% (20 meV) for H$_2$O and 9% (11 meV) for NH$_3$. The effects become
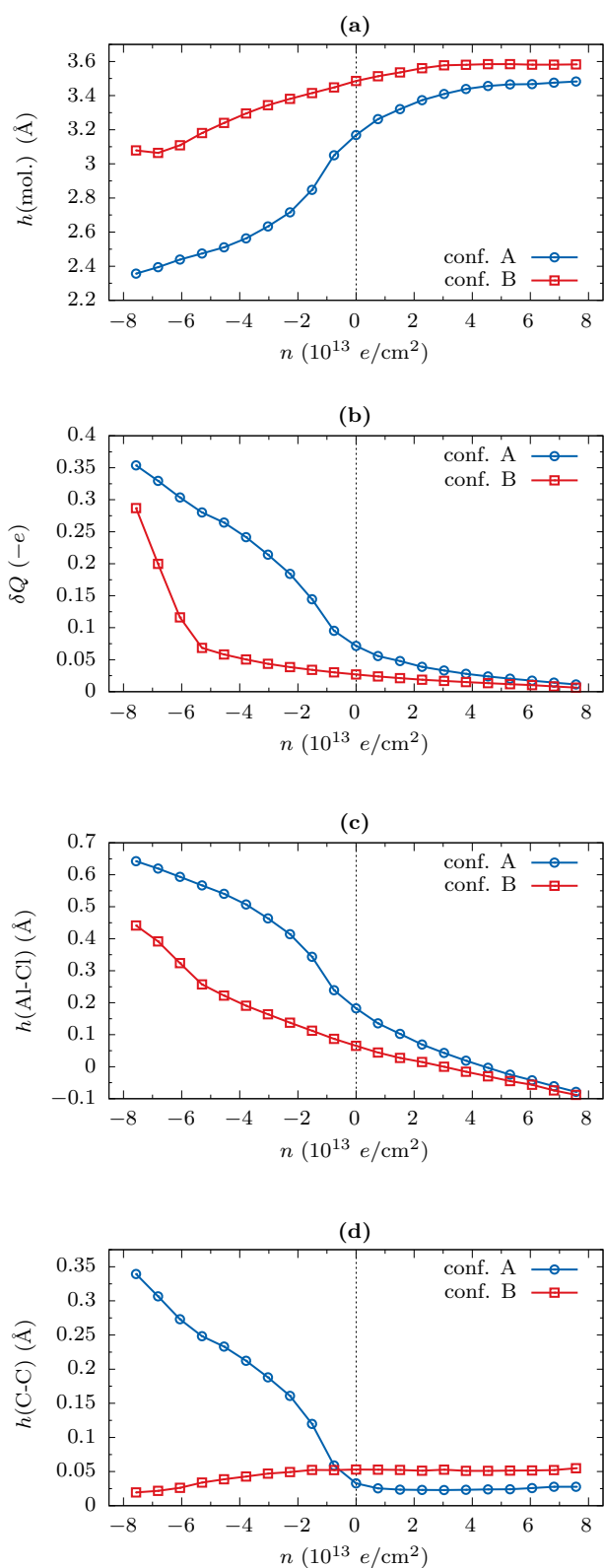
8

(a)

(b)

(c)

(d)

Figure 10: (a) Vertical separation of the molecule from the graphene. (b) Charge transfer between $AlCl_3$ and graphene given by Equation (3). (c) Vertical separation between Al and Cl atoms in $AlCl_3$. (d) Vertical separation between C atoms in graphene.

Table 1: Absolute and relative change in the adsorption energy facilitated by differed doping regimes in graphene.

			$\times 10^{12}$ e/cm^2		$\times 10^{13}$ e/cm^2	
			n-type	p-type	n-type	p-type
H_2	Δ(abs.)[a]	(meV)	<1	<1	3	14
	Δ(rel.)[b]	(%)	<1	<1	4	22
H_2O	Δ(abs.)	(meV)	20	13	173	207
	Δ(rel.)	(%)	16	10	138	165
NH_3	Δ(abs.)	(meV)	11	11	113	214
	Δ(rel.)	(%)	9	8	90	171
$AlCl_3$	Δ(abs.)	(meV)	3	9	266	251
	Δ(rel.)	(%)	<1	2	58	55

[a] Δ(abs.) is calculated using Equation (4). [b] Δ(rel.) is calculated using Equation (5).

centrations may not be universally significant, the sheet's response is critically dependent on molecular coverage, which is highly sensitive to adsorption energy. Thus, even at 10^{12} e/cm^2, the modulation of adsorption interactions could significantly affect the effective sensitivity, given sufficient molecule-sheet charge transfers. On the other hand, at 10^{13} e/cm^2, the impact on adsorption becomes substantial enough to be considered universally significant, with implications for surface catalysis, heterostructure fabrication, energy storage, and environmental monitoring. Given the mechanism by which the doping affects in interactions with H_2O and NH_3, comparable modulation may be also possible for H_2S, NO_2, SO_2, PH_3, and other similar species.

In the case of $AlCl_3$, doping graphene at a level of 10^{12} e/cm^2 has a relatively low impact on the adsorption of the molecule, with changes in adsorption energy of 2% (9 meV) or less. Given the already strong interaction, this modulation is generally negligible. However, at higher doping levels of 10^{13} e/cm^2, the effects become quite substantial, with n-type doping resulting in a 58% (266 meV) change and p-type doping leading to a comparable 55% (251 meV). Consequently, at such doping levels, the effect on the adsorption of $AlCl_3$ should be considered significant, potentially influencing the growth of metal oxides, such as Al_2O_3, on graphene surfaces. Given the mechanism by which doping affects interactions with $AlCl_3$, similar modulation may also be possible for other Lewis acids, such as $Al(CH_3)_3$, $Al(OH)_3$, and BF_3.

4. Conclusions

This study elucidates the intricate impact of carrier concentration on the interaction between molecular adsorbates and graphene. By employing DFT methods, we examined how the adsorption of various species evolves for graphene doping concentrations between -7.57×10^{13} e/cm^2 and 7.57×10^{13} e/cm^2, revealing distinct patterns of changes characteristic to each adsorbate. The effects of charge carrier concentration in graphene are shown to be intrinsic to the adsorbed species, due to the unique underlying chemistry that modulates the interaction in response to varying charge availability on the graphene's surface.

This complex interplay makes carrier concentration a powerful and selective tool for modulating the interaction between molecular adsorbates and graphene. The effects are tunable and evident for both n-type and p-type doping. Low-to-medium doping levels ($\pm 10^{12}$ e/cm^2) show modest modulation, whereas high doping levels ($\pm 10^{13}$ e/cm^2) yield substantial enhancements, with interaction strength increases exceeding 150% and hundreds of meV. Moreover, the molecule-specific nature of these effects highlights the versatility of carrier concentration as a tool for tailoring graphene's surface chemistry. This modulation is crucial for advancing applications where precise control over molecular interactions is essential.

Consequently, the insights gained from this study not only deepen our understanding of graphene's surface chemistry but also pave the way for innovative applications in sensing, catalysis, and beyond. The ability to modulate molecular adsorption through charge carrier concentration offers a powerful tool for enhancing the functionality and versatility of graphene-based materials.

even more substantial at doping levels on the order of 10^{13} e/cm^2. In this regime, p-type doping is shown to be more effective in modulating the adsorption interaction for both H_2O and NH_3, resulting in substantial enhancements of 165% (207 meV) and 171% (214 meV) for H_2O and NH_3, respectively. Consequently, while 10^{12} e/cm^2 doping con-

9

Acknowledgments

References

[1] A. H. Castro Neto, F. Guinea, N. M. R. Peres, K. S. Novoselov and A. K. Geim, The electronic properties of graphene, Rev. Mod. Phys. 81 (2009) 109–162. doi:10.1103/RevModPhys.81.109.

[2] A. A. Balandin, Thermal properties of graphene and nanostructured carbon materials, Nature Materials 10 (8) (2011) 569–581. doi:10.1038/nmat3064.

[3] D. G. Papageorgiou, I. A. Kinloch and R. J. Young, Mechanical properties of graphene and graphene-based nanocomposites, Progress in Materials Science 90 (2017) 75–127. doi:https://doi.org/10.1016/j.pmatsci.2017.07.004.

[4] L. Syam Sundar, M. Amin Mir, M. Waqar Ashraf and F. Djavanroodi, Synthesis and characterization of graphene and its composites for lithium-ion battery applications: A comprehensive review, Alexandria Engineering Journal 78 (2023) 224–245. doi:https://doi.org/10.1016/j.aej.2023.07.044.

[5] X. Lu, M. Cai, X. Wu, Y. Zhang, S. Li, S. Liao and X. Lu, Controllable synthesis of 2D materials by electrochemical exfoliation for energy storage and conversion application, Small 19 (9) (2023) 2206702. arXiv:https://onlinelibrary.wiley.com/doi/pdf/10.1002/smll.202206702, doi:https://doi.org/10.1002/smll.202206702.

[6] E. Muchuweni and E. T. Mombeshora, Recent advances in thermoelectric performance by incorporating graphene-based materials for energy harvesting, Renewable Energy Focus 45 (2023) 40–52. doi:https://doi.org/10.1016/j.ref.2023.02.005.

[7] X. Zhuang, J. Liu, S. Zhong and L. Ma, Selective catalysis for the reductive amination of furfural toward furfurylamine by graphene-co-shelled cobalt nanoparticles, Green Chem. 24 (2022) 271–284. doi:10.1039/D1GC03578A.

[8] Q. Wang, H. Liang, J. Zhou, J. Wang, Z. Ye, M. Zhao, H. Yang, Y. Song et al, Boosting oxygen reduction catalysis by introducing Fe bridging atoms between Pt nanoparticles and N-doped graphene, Chemical Engineering Journal 467 (2023) 143482. doi:https://doi.org/10.1016/j.cej.2023.143482.

[9] H. Dan, Y. Gao, L. Feng, W. Yin, X. Xu, B. Gao and Q. Yue, Superamphiphilic graphene promotes peroxymonosulfate-based emulsion catalysis for efficient oil purification, Journal of Hazardous Materials 445 (2023) 130469. doi:https://doi.org/10.1016/j.jhazmat.2022.130469.

[10] C. Yang, C. Yang, Y. Guo, J. Feng and X. Guo, Graphene–molecule–graphene single-molecule junctions to detect electronic reactions at the molecular scale, Nature Protocols 18 (6) (2023) 1958–1978. doi:10.1038/s41596-023-00822-x.

[11] Q. Li, M. Sun, C. Jiang, S. Song, T. Li, M. Xu, W. Chen and H. Peng, Phosphorus doping of graphene for conductometric room temperature ammonia sensing, Sensors and Actuators B: Chemical 379 (2023) 133234. doi:https://doi.org/10.1016/j.snb.2022.133234.

[12] X. Fan, D. Moreno-Garcia, J. Ding, K. B. Gylfason, L. G. Villanueva and F. Niklaus, Resonant transducers consisting of graphene ribbons with attached proof masses for NEMS sensors, ACS Applied Nano Materials 7 (1) (2024) 102–109. arXiv:https://doi.org/10.1021/acsanm.3c03642, doi:10.1021/acsanm.3c03642.

[13] J. Wang, Y. Zheng, S. Qiu and L. Song, Ethanol inducing self-assembly of poly-(thioctic acid)/graphene supramolecular ionomers for healable, flame-retardant, shape-memory electronic devices, Journal of Colloid and Interface Science 629 (2023) 908–915. doi:https://doi.org/10.1016/j.jcis.2022.09.037.

[14] J. Díez-Mérida, A. Díez-Carlón, S. Y. Yang, Y.-M. Xie, X.-J. Gao, J. Senior, K. Watanabe, T. Taniguchi et al, Symmetry-broken josephson junctions and superconducting diodes in magic-angle twisted bilayer graphene, Nature Communications 14 (1) (2023) 2396. doi:10.1038/s41467-023-38005-7.

[15] C. Backes, A. M. Abdelkader, C. Alonso, A. Andrieux-Ledier, R. Arenal, J. Azpeitia, N. Balakrishnan, L. Banszerus et al, Production and processing of graphene and related materials, 2D Materials 7 (2) (2020) 022001. doi:10.1088/2053-1583/ab1e0a.

[16] S. Fukamachi, P. Solís-Fernández, K. Kawahara, D. Tanaka, T. Otake, Y.-C. Lin, K. Suenaga and H. Ago, Large-area synthesis and transfer of multilayer hexagonal boron nitride for enhanced graphene device arrays, Nature Electronics 6 (2) (2023) 126–136. doi:10.1038/s41928-022-00911-x.

[17] S. Zhang, L. Wang, Y. Luo, K. Wang, X. Feng, Y. Pei, H. Wu, Y. Li et al, A convenient, low-cost graphene UV-cured additive manufacturing electronic process to achieve flexible sensors, Chemical Engineering Journal 451 (2023) 138521. doi:https://doi.org/10.1016/j.cej.2022.138521.

[18] J. Zhao, P. Ji, Y. Li, R. Li, K. Zhang, H. Tian, K. Yu, B. Bian et al, Ultrahigh-mobility semiconducting epitaxial graphene on silicon carbide, Nature 625 (7993) (2024) 60–65. doi:10.1038/s41586-023-06811-0.

[19] A. Pradeepkumar, D. Cortie, E. Smyth, A. P. Le Brun and F. Iacopi, Epitaxial graphene growth on cubic silicon carbide on silicon with high temperature neutron reflectometry: an operando study, RSC Adv. 14 (2024) 3232–3240. doi:10.1039/D3RA08289J.

[20] T. Ciuk, L. Ciura, P. Michałowski, J. Jagiełło, A. Dobrowolski, K. Piętak, D. Kalita, M. Wzorek et al, Contamination-induced inhomogeneity of noise sources distribution in Al_2O_3-passivated quasi-free-standing graphene on 4H-SiC(0001), Physica E: Low-dimensional Systems and Nanostructures 142 (2022) 115264. doi:https://doi.org/10.1016/j.physe.2022.115264.

[21] A. Dobrowolski, J. Jagiełło, T. Ciuk, K. Piętak and E. B. Możdżyńska, Layer-resolved raman imaging and analysis of parasitic ad-layers in transferred graphene, Applied Surface Science 608 (2023) 155054. doi:https://doi.org/10.1016/j.apsusc.2022.155054.

[22] A. Dobrowolski, J. Jagiełło, K. Piętak-Jurczak, M. Wzorek, D. Czołak and T. Ciuk, Spectroscopic properties of close-to-perfect-monolayer quasi-free-standing epitaxial graphene on 6H-SiC(0001), Applied Surface Science 642 (2024) 158617. doi:https://doi.org/10.1016/j.apsusc.2023.158617.

[23] G. Cui, Z. Peng, X. Chen, Y. Cheng, L. Lu, S. Cao, S. Ji, G. Qu et al, Freestanding graphene fabric film for flexible infrared camouflage, Advanced Science 9 (5) (2022) 2105004. arXiv:https://onlinelibrary.wiley.com/doi/pdf/10.1002/advs.202105004, doi:https://doi.org/10.1002/advs.202105004.

[24] S. El-Ahmar, M. J. Szary, T. Ciuk, R. Prokopowicz, A. Dobrowolski, J. Jagiełło and M. Ziemba, Graphene on SiC as a promising platform for magnetic field detection under neutron irradiation, Applied Surface Science 590 (2022) 152992. doi:https://doi.org/10.1016/j.apsusc.2022.152992.

[25] J. Pang, S. Peng, C. Hou, H. Zhao, Y. Fan, C. Ye, N. Zhang, T. Wang et al, Applications of graphene in five senses, nervous system, and artificial muscles, ACS Sensors 8 (2) (2023) 482–514, pMID: 36656873. arXiv:https://doi.org/10.1021/acssensors.2c02790, doi:10.1021/acssensors.2c02790.

[26] T. Yin, L. Xu, B. Gil, N. Merali, M. S. Sokolikova, D. C. A. Gaboriau, D. S. K. Liu, A. N. Muhammad Mustafa et al, Graphene sensor arrays for rapid and accurate detection of pancreatic cancer exosomes in patients' blood plasma samples, ACS Nano 17 (15) (2023) 14619–14631, pMID: 37470391. arXiv:https://doi.org/10.1021/acsnano.3c01812, doi:10.1021/acsnano.3c01812.

[27] M. Kong, M. Yang, R. Li, Y.-Z. Long, J. Zhang, X. Huang, X. Cui, Y. Zhang et al, Graphene-based flexible wearable sensors: mechanisms, challenges, and future directions, The International Journal of Advanced Manufacturing Technology 131 (5) (2024) 3205–3237. doi:10.1007/s00170-023-12007-7.

[28] R. Kumar, S. Sahoo, E. Joanni, R. K. Singh and R. M. Yadav, Graphene-metal oxide hybrid materials with 2D and 3D morphologies for advanced supercapacitor electrodes: Status, challenges and prospects, Materials Today Nano 24 (2023) 100399. doi:https://doi.org/10.1016/j.mtnano.2023.100399.

[29] M. A. Iqbal, N. Anwar, M. Malik, M. Al-Bahrani, M. R. Islam, J. R. Choi, P. V. Pham and X. Liu, Nanostructures/graphene/silicon junction-based high-performance photodetection systems: Progress, challenges, and future trends, Advanced Materials Interfaces 10 (7) (2023) 2202208. arXiv:https://onlinelibrary.wiley.com/doi/pdf/10.1002/admi.202202208, doi:https://doi.org/10.1002/admi.202202208.

[30] D. Somvanshi and S. Jit, Advances in 2D materials based mixed-dimensional heterostructures photodetectors: Present status and challenges, Materials Science in Semiconductor Processing 164 (2023) 107598. doi:https://doi.org/10.1016/j.mssp.2023.107598.

[31] J. Gao, J. Zhao and F. Ding, Transition metal surface passivation induced

graphene edge reconstruction, Journal of the American Chemical Society 134 (14) (2012) 6204–6209, pMID: 22420470. `arXiv:https://doi.org/10.1021/ja2104119, doi:10.1021/ja2104119`.

[32] Q. Wang, R. Pang and X. Shi, Molecular precursor induced surface reconstruction at graphene/Pt(111) interfaces, The Journal of Physical Chemistry C 119 (39) (2015) 22534–22541. `arXiv:https://doi.org/10.1021/acs.jpcc.5b06842, doi:10.1021/acs.jpcc.5b06842`.

[33] C. Romero-Muñiz, A. Martín-Recio, P. Pou, J. M. Gómez-Rodríguez and R. Pérez, Substrate-induced enhancement of the chemical reactivity in metal-supported graphene, Phys. Chem. Chem. Phys. 20 (2018) 19492–19499. `doi:10.1039/C8CP02827C`.

[34] M. Kolmer, J. Hall, S. Chen, S. Roberts, Z. Fei, Y. Han and M. C. Tringides, Atomic-scale manipulation of buried graphene–silicon carbide interface by local electric field, Communications Physics 7 (1) (2024) 16. `doi:10.1038/s42005-023-01515-3`.

[35] C. Riedl, C. Coletti, T. Iwasaki, A. A. Zakharov and U. Starke, Quasi-free-standing epitaxial graphene on sic obtained by hydrogen intercalation, Phys. Rev. Lett. 103 (2009) 246804. `doi:10.1103/PhysRevLett.103.246804`.

[36] I. Palacio, G. Otero-Irurueta, C. Alonso, J. I. Martínez, E. López-Elvira, I. Muñoz-Ochando, H. J. Salavagione, M. F. López et al, Chemistry below graphene: Decoupling epitaxial graphene from metals by potential-controlled electrochemical oxidation, Carbon 129 (2018) 837–846. `doi:https://doi.org/10.1016/j.carbon.2017.12.104`.

[37] M. J. Szary, S. El-Ahmar and T. Ciuk, The impact of partial H intercalation on the quasi-free-standing properties of graphene on SiC(0001), Applied Surface Science 541 (2021) 148668. `doi:https://doi.org/10.1016/j.apsusc.2020.148668`.

[38] J. Wang, M. Kim, L. Chen, K.-M. Ho, M. Tringides, C.-Z. Wang and S. Wang, Manipulation of electronic property of epitaxial graphene on SiC substrate by Pb intercalation, Phys. Rev. B 103 (2021) 085403. `doi:10.1103/PhysRevB.103.085403`.

[39] Y. Kim, H. Han, D. Luo, R. S. Ruoff and H.-J. Shin, Decoupling of CVD-grown epitaxial graphene using NaCl intercalation, Nanoscale 14 (2022) 16929–16935. `doi:10.1039/D2NR05660G`.

[40] S. Y. F. Zhao, G. A. Elbaz, D. K. Bediako, C. Yu, D. K. Efetov, Y. Guo, J. Ravichandran, K.-A. Min et al, Controlled electrochemical intercalation of graphene/h-BN van der waals heterostructures, Nano Letters 18 (1) (2018) 460–466, pMID: 29268017. `arXiv:https://doi.org/10.1021/acs.nanolett.7b04396, doi:10.1021/acs.nanolett.7b04396`.

[41] S. Mammadov, J. Ristein, J. Krone, C. Raidel, M. Wanke, V. Wiesmann, F. Speck and T. Seyller, Work function of graphene multilayers on SiC(0001), 2D Materials 4 (1) (2017) 015043. `doi:10.1088/2053-1583/4/1/015043`.

[42] S. Vaziri, V. Chen, L. Cai, Y. Jiang, M. E. Chen, R. W. Grady, X. Zheng and E. Pop, Ultrahigh doping of graphene using flame-deposited moo3, IEEE Electron Device Letters 41 (10) (2020) 1592–1595. `doi:10.1109/LED.2020.3018485`.

[43] M. S. Choi, A. Nipane, B. S. Y. Kim, M. E. Ziffer, I. Datta, A. Borah, Y. Jung, B. Kim et al, High carrier mobility in graphene doped using a monolayer of tungsten oxyselenide, Nature Electronics 4 (10) (2021) 731–739. `doi:10.1038/s41928-021-00657-y`.

[44] A. Pramanik, S. Thakur, B. Singh, P. Willke, M. Wenderoth, H. Hofsäss, G. Di Santo, L. Petaccia et al, Anomalies at the dirac point in graphene and its hole-doped compositions, Phys. Rev. Lett. 128 (2022) 166401. `doi:10.1103/PhysRevLett.128.166401`.

[45] F. Karimi, S. Mitra, S. Soleimanikahnoj and I. Knezevic, Plasmon-enhanced optical nonlinearity in graphene nanomeshes, Phys. Rev. B 108 (2023) 035414. `doi:10.1103/PhysRevB.108.035414`.

[46] T. Ciuk, W. Kaszub, K. Kosciewicz, A. Dobrowolski, J. Jagiello, A. Chamryga, J. Gaca, M. Wojcik et al, Highly-doped p-type few-layer graphene on UID off-axis homoepitaxial 4h–sic, Current Applied Physics 27 (2021) 17–24. `doi:https://doi.org/10.1016/j.cap.2021.03.021`.

[47] P. Rosenzweig, H. Karakachian, D. Marchenko and U. Starke, Surface charge-transfer doping a quantum-confined silver monolayer beneath epitaxial graphene, Phys. Rev. B 105 (2022) 235428. `doi:10.1103/PhysRevB.105.235428`.

[48] T. Ciuk and W. Strupinski, Statistics of epitaxial graphene for hall effect sensors, Carbon 93 (2015) 1042–1049. `doi:https://doi.org/10.1016/j.carbon.2015.06.032`.

[49] K. H. Kim, H. He, C. Struzzi, A. Zakharov, C. E. Giusca, A. Tzalenchuk, Y. W. Park, R. Yakimova et al, Ambipolar charge transport in quasi-free-standing monolayer graphene on SiC obtained by gold intercalation, Phys. Rev. B 102 (2020) 165403. `doi:10.1103/PhysRevB.102.165403`.

[50] S. El-Ahmar, M. Przychodnia, J. Jankowski, R. Prokopowicz, M. Ziemba,

[51] M. J. Szary, W. Reddig, J. Jagiełło et al, The comparison of InSb-based thin films and graphene on SiC for magnetic diagnostics under extreme conditions, Sensors 22 (14) (2022).

[51] T. Ciuk, R. Kozłowski, A. Romanowska, A. Zagojski, K. Piętak-Jurczak, B. Stańczyk, K. Przyborowska, D. Czołak et al, Defect-engineered graphene-on-silicon-carbide platform for magnetic field sensing at greatly elevated temperatures, Carbon Trends 13 (2023) 100303. `doi:https://doi.org/10.1016/j.cartre.2023.100303`.

[52] M. J. Szary and P. Radomski, Unveiling the chemical underpinnings behind the enhanced adsorption interaction of NO_2 on MoS_2, $MoSe_2$, and $MoTe_2$ transition metal dichalcogenides, The Journal of Physical Chemistry C 127 (43) (2023) 21374–21386. `arXiv:https://doi.org/10.1021/acs.jpcc.3c05101, doi:10.1021/acs.jpcc.3c05101`.

[53] P. Radomski and M. J. Szary, Transition metals vs. chalcogens: The impact on NO_x adsorption on MoS_2, $MoSe_2$ and WS_2 transition-metal dichalcogenides, Acta Materialia 272 (2024) 119949. `doi:https://doi.org/10.1016/j.actamat.2024.119949`.

[54] M. J. Szary, Toward high selectivity of sensor arrays: Enhanced adsorption interaction and selectivity of gas detection (N_2, O_2, NO, CO, CO_2, NO_2, SO_2, AlH_3, NH_3, and PH_3) on transition metal dichalcogenides (MoS_2, $MoSe_2$, and $MoTe_2$), Acta Materialia 274 (2024) 120016. `doi:https://doi.org/10.1016/j.actamat.2024.120016`.

[55] G. Yu, Y. Xie, Q. Ge, Q. Dai, J. Xu and H. Cao, Mechanism of ozone adsorption and activation on B-, N-, P-, and Si-doped graphene: A DFT study, Chemical Engineering Journal 430 (2022) 133114. `doi:https://doi.org/10.1016/j.cej.2021.133114`.

[56] A. I. Ayesh, The effect of ZrO_x modification of graphene nanoribbon on its adsorption for NO_x: A DFT investigation, Materials Chemistry and Physics 291 (2022) 126693. `doi:https://doi.org/10.1016/j.matchemphys.2022.126693`.

[57] M. A. A. Ibrahim, M. H. A. Hamad, A. H. M. Mahmoud, G. A. H. Mekhemer, P. A. Sidhom, S. R. M. Sayed, N. A. M. Moussa, A. I. M. Rabee et al, Adsorption of favipiravir on pristine graphene nanosheets as a drug delivery system: a DFT study, RSC Adv. 13 (2023) 17465–17475. `doi:10.1039/D3RA03227B`.

[58] M. Heshami, Z. Tavangar and B. Taheri, Adsorption of gold and silver glycinate on graphene and graphene oxide surface: A DFT study, Applied Surface Science 619 (2023) 156676. `doi:https://doi.org/10.1016/j.apsusc.2023.156676`.

[59] S. S. Dindorkar, N. Sinha and A. Yadav, Comparative study on adsorption of volatile organic compounds on graphene, boron nitride and boron carbon nitride nanosheets, Solid State Communications 359 (2023) 115021. `doi:https://doi.org/10.1016/j.ssc.2022.115021`.

[60] N. M. Caffrey, R. Armiento, R. Yakimova and I. A. Abrikosov, Changes in work function due to no2 adsorption on monolayer and bilayer epitaxial graphene on sic(0001), Phys. Rev. B 94 (2016) 205411. `doi:10.1103/PhysRevB.94.205411`.

[61] M. Stachová, M. Dubecký and F. Karlický, Adsorption of atomic and molecular monolayers on Pt-supported graphene, Chemical Physics 564 (2023) 111713. `doi:https://doi.org/10.1016/j.chemphys.2022.111713`.

[62] L. Bengtsson, Dipole correction for surface supercell calculations, Phys. Rev. B 59 (1999) 12301–12304. `doi:10.1103/PhysRevB.59.12301`.

[63] P. Giannozzi, S. Baroni, N. Bonini, M. Calandra, R. Car, C. Cavazzoni, D. Ceresoli, G. L. Chiarotti et al, QUANTUM ESPRESSO: a modular and open-source software project for quantum simulations of materials, Journal of Physics: Condensed Matter 21 (39) (2009) 395502. `doi:10.1088/0953-8984/21/39/395502`.

[64] P. Giannozzi, O. Andreussi, T. Brumme, O. Bunau, M. B. Nardelli, M. Calandra, R. Car, C. Cavazzoni et al, Advanced capabilities for materials modelling with QUANTUM ESPRESSO, Journal of Physics: Condensed Matter 29 (46) (2017) 465901.

[65] P. Giannozzi, O. Baseggio, P. Bonfà, D. Brunato, R. Car, I. Carnimeo, C. Cavazzoni, S. de Gironcoli et al, QUANTUM ESPRESSO toward the exascale, The Journal of Chemical Physics 152 (15) (2020) 154105. `arXiv:https://doi.org/10.1063/5.0005082, doi:10.1063/5.0005082`.

[66] H. J. Monkhorst and J. D. Pack, Special points for brillouin-zone integrations, Phys. Rev. B 13 (1976) 5188–5192. `doi:10.1103/PhysRevB.13.5188`.

[67] J. P. Perdew, K. Burke and M. Ernzerhof, Generalized gradient approximation made simple, Phys. Rev. Lett. 77 (1996) 3865–3868. `doi:10.1103/PhysRevLett.77.3865`.

[68] J. P. Perdew, A. Ruzsinszky, G. I. Csonka, O. A. Vydrov, G. E. Scuseria, L. A. Constantin, X. Zhou and K. Burke, Restoring the density-gradient expansion for exchange in solids and surfaces, Phys. Rev. Lett. 100 (2008) 136406. `doi:10.1103/PhysRevLett.100.136406`.

[69] J. Heyd, G. E. Scuseria and M. Ernzerhof, Hybrid functionals based on a screened Coulomb potential, The Journal of Chemical Physics 118 (18) (2003) 8207–8215. `doi:10.1063/1.1564060`.

[70] A. Kokalj, XCrySDen–a new program for displaying crystalline structures and electron densities, Journal of Molecular Graphics and Modelling 17 (3) (1999) 176 – 179. `doi:https://doi.org/10.1016/S1093-3263(99)00028-5`.

[71] F. Banhart, J. Kotakoski and A. V. Krasheninnikov, Structural defects in graphene, ACS Nano 5 (1) (2011) 26–41, pMID: 21090760. `arXiv:https://doi.org/10.1021/nn102598m, doi:10.1021/nn102598m`.

[72] S. Mammadov, J. Ristein, R. J. Koch, M. Ostler, C. Raidel, M. Wanke, R. Vasiliauskas, R. Yakimova et al, Polarization doping of graphene on silicon carbide, 2D Materials 1 (3) (2014) 035003. `doi:10.1088/2053-1583/1/3/035003`.

[73] J. Sławińska, H. Aramberri, M. Muñoz and J. Cerdá, Ab initio study of the relationship between spontaneous polarization and p-type doping in quasi-freestanding graphene on H-passivated SiC surfaces, Carbon 93 (2015) 88–104. `doi:https://doi.org/10.1016/j.carbon.2015.05.025`.

[74] V. M. Bermudez, Theoretical study of the adsorption of lewis acids on mos_2 in relation to atomic layer deposition of al_2o_3, Journal of Vacuum Science & Technology A 38 (6) (2020) 062412. `arXiv:https://pubs.aip.org/avs/jva/article-pdf/doi/10.1116/6.0000467/15819780/062412\_1\_online.pdf, doi:10.1116/6.0000467`.

12